

Linear dichroic soft X-ray microscopy of ferroelectric stripe domains in epitaxial $\text{K}_{0.6}\text{Na}_{0.4}\text{NbO}_3$

M. Schneider,¹ T. A. Butcher,^{1,*} S. Wagner,¹ D. Metternich,^{1,2,3} C. Klose,¹ E. Malm,⁴ R. Battistelli,^{2,3} V. Deinhart,¹ J. Fuchs,¹ S. Wittrock,² T. Karaman,^{2,3} K. Puzhekadavil Joy,^{2,3} M. Patras,^{2,3} F. Büttner,^{2,3} S. Wintz,² M. Weigand,² C. M. Günther,⁵ D. Engel,¹ P. Gaal,^{6,7} J. Schwarzkopf,⁶ B. Pfau,¹ and S. Eisebitt^{1,8}

¹*Max Born Institute for Nonlinear Optics and Short Pulse Spectroscopy, 12489 Berlin, Germany*

²*Helmholtz-Zentrum Berlin für Materialien und Energie, 14109 Berlin, Germany*

³*Experimental Physics V, Center for Electronic Correlations and Magnetism, University of Augsburg, 86159 Augsburg, Germany*

⁴*MAX IV, Lund University, 224 84 Lund, Sweden*

⁵*Technische Universität Berlin, Zentraleinrichtung Elektronenmikroskopie, 10623 Berlin, Germany*

⁶*Leibniz-Institut für Kristallzüchtung, Max-Born-Straße 2, 12489 Berlin, Germany*

⁷*TXproducts UG, Luruper Hauptstrasse 1, 22547 Hamburg, Germany*

⁸*Technische Universität Berlin, Institut für Physik und Astronomie,*

Straße des 17. Juni 135, 10623 Berlin, Germany

(Dated: March 17, 2026)

Functional properties of ferroelectric thin films are governed by domains that can be engineered by epitaxial strain. Soft X-ray microscopy can image domain structures with elemental and electronic sensitivity, but hitherto its application to strain-stabilized domains has been hindered by the absorption of soft X-rays in epitaxial substrates. Here, it is demonstrated how this limitation can be overcome by locally back-thinning the (110) TbScO_3 substrate of epitaxial $\text{K}_{0.6}\text{Na}_{0.4}\text{NbO}_3$ ferroelectric thin films to achieve soft X-ray transparency at the O K-edge around 530 eV. Strain-induced ferroelectric stripe domains with periods down to 44 nm were resolved by scanning transmission X-ray microscopy and coherent diffractive imaging by exploiting the X-ray linear dichroism of hybridized O 2p–Nb 4d states, providing sensitivity to in-plane polarization components under normal incidence. The results establish soft X-ray microscopy for nanoscale imaging of epitaxial ferroelectric domains structures and open perspectives for time-resolved studies thereof.

Functional properties of ferroelectric materials such as piezoelectricity, flexoelectricity, and photoelectric performance depend on the arrangement, orientation and size of the ferroelectric domains and their domain walls [1, 2]. Domain formation is governed by mechanical and electrical boundary conditions of the films, which can be engineered in epitaxial thin films by using lattice mismatched substrates and the application of electrode layers, respectively. As the size of ferroelectric domains in thin films is on the nanoscale, microscopy methods with high spatial resolutions are required for their study. The common approach is piezoresponse force microscopy (PFM) with usual spatial resolutions around 20 nm [3]. Alternative and complementary characterization techniques with high spatial resolution are X-ray microscopy on the nanoscale or transmission electron microscopy (TEM) on the unit cell level. The latter is impractical for extended regions of ferroelectric domains in standard setups [4].

The availability of high coherent flux and tunable photon energies at synchrotron light sources has enabled imaging of ferroelectric order both in the hard and soft X-ray energy regimes. High resolution X-ray microscopy can be separated into three approaches: Firstly, full-field techniques that provide direct images such as X-ray photo-emission electron microscopy (X-PEEM) [5]

or dark field X-ray microscopy [6, 7]. Secondly, scanning microscopy relying on focusing the X-rays to a sub-100 nm diameter spot, which is usually achieved by Fresnel zone plates (FZPs). Thirdly, methods based on the reconstruction of real space images from coherent diffraction patterns by coherent diffractive imaging (CDI) techniques. Regarding hard X-rays, information about ferroelectric domain structures is encoded in alterations of Bragg peaks. This structural information can be related to ferroelectric domains by mapping the Bragg peaks in nanoprobe measurements with FZP focused hard X-ray beams in reflection geometry [8–10]. Less well established is the imaging of ferroelectric domain structures with the CDI approach of Bragg ptychography, which has been employed for imaging out-of-plane ferroelectric polarization with sub-10 nm spatial resolution [11].

Soft X-ray microscopy relies on X-ray beams with lower photon energies between 200–2000 eV and a higher coherent fraction than hard X-rays. Contrast mechanisms arise due to electronic transitions at elemental X-ray absorption edges contained in this energy range. As ferroelectrics are predominately oxides, the O K-edge around 530 eV with the transition of 1s→2p is of high relevance for their study. This transition provides strong sensitivities to anisotropic charge distributions in the unit cell as well as the hybridization of O 2p orbitals with metal states, which can yield the ferroelectric domain structures by X-ray linear dichroism (XLD). Linear dichroic imaging senses the axis of the ferroelectric polarization

* tim.butcher@mbi-berlin.de

relative to the plane of polarization of the X-ray beam. At the O K-edge, this was first carried out with surface sensitive X-PEEM [5] and recently by the CDI method of soft X-ray ptychography [12] in multiferroic BiFeO₃ (BFO) [13]. Strong absorption of soft X-rays at the elemental absorption edges restricts the sample thicknesses to sub-200 nm for high resolution soft X-ray microscopy that is performed in transmission, which has limited linear dichroic imaging to membranes of ferroic oxides [13–16]. This limitation has so far prevented the application of linear dichroic soft X-ray microscopy to epitaxial thin films in their as-grown state on substrates.

Previous studies with soft X-ray ptychography were carried out on freestanding BFO films [13, 16], which invariably form ferroelectric mosaic domains due to the lack of epitaxial strain. However, the stabilization of ferroelectric phases in new materials and useful domain structures relies on epitaxial strain from a substrate. Imaging such epitaxially stabilized domain structures by soft X-ray microscopy therefore requires a transmission geometry compatible with thick oxide substrates. Here, this challenge is addressed for the first time.

An ongoing search for new ferroelectric materials has ensued due to the presence of toxic lead in common Pb[Zr_xTi_{1-x}]O₃ (PZT). One promising lead-free candidate is K_xNa_{1-x}NbO₃. It was first shown in the 1950s that a solid solution of ferroelectric KNbO₃ and antiferroelectric NaNbO₃ induces a ferroelectric phase, which was then refined for piezoelectric applications approximately 50 years thereafter with an equal share of the constituents as K_{0.5}Na_{0.5}NbO₃ [17]. Several phases are now available in thin film form with favorable ferroelectric properties due to their high Curie temperature of 690 K, polarization (33 μC cm⁻²) and piezoelectric coefficient (0.454).

In the following, an imaging study of ferroelectric K_{0.6}Na_{0.4}NbO₃ (KNN) thin films on (110) TbScO₃ (TSO) substrates by means of scanning transmission X-ray microscopy (STXM) and holography-assisted CDI at the O K-edge, is presented. The strongly anisotropic strain conditions of the TSO substrate lead to the formation of four different monoclinic superdomains consisting of periodic 90° ferroelectric stripe domain arrangements with the alignment of domain walls in the [11̄2]_{TSO} or [1̄12]_{TSO} orthorhombic directions of the TSO substrate [8, 18–20]. Charge neutrality at the domain walls and neighboring superdomains forces the ferroelectric in-plane polarization of the stripe domains to point along [11̄0]_{TSO} or [001]_{TSO}. It follows that the effective ferroelectric polarization of each superdomain is oriented along the propagation direction of its ferroelectric stripe domains.

The pseudocubic unit cell of KNN is displayed in Fig. 1(a) with the O²⁻ octahedra surrounding the central Nb in the perovskite structure. The ferroelectricity of KNN largely originates in the off-center displacement of the pentavalent Nb⁵⁺ cation inside the O²⁻ octahedra [21]. It follows that the ferroelectric order is amenable to dichroic imaging at the O K-edge, which is sensitive to

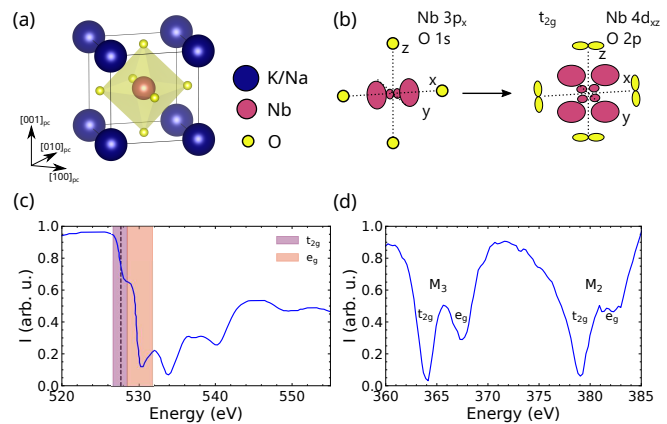


FIG. 1. (a) The pseudocubic (pc) perovskite unit cell of KNN shows the octahedral coordination of Nb⁵⁺ by O²⁻. (b) Sketch of the electronic orbitals in the ground (left) and excited hybridized state (right). The anisotropy in the O 2p orbitals causes strong XLD at the O K-edge. (c) X-ray transmission spectrum of 37 nm KNN on TSO at the O K-edge. The peaks assigned to hybridization with 4d t_{2g} and e_g are shaded. The broken vertical line indicates the photon energy of maximum XLD. (d) X-ray transmission spectrum of 37 nm KNN on TSO at the Nb M_{3,2}-edges.

the O 2p-Nb 4d hybridized excited states [22–29], analogously to ferroelectrics with 3d transition metals such as BFO [5, 13]. In octahedral symmetry, the 4d states can point in direction of the O²⁻ ions (e_g) or in between them (t_{2g}). The excitation process is shown schematically in Fig. 1(b) with the spherical O 1s and the Nb 3p states adjacent to one of the t_{2g} hybridized state, which consists of the O 2p and Nb 4d_{xz} in the sketch. The anisotropic O 2p orbitals cause the XLD by preferential absorption of X-rays with linear polarization parallel to the asymmetry in charge distribution. Under normal incidence of the X-rays, the in-plane projection of the ferroelectric polarization in the thin film can be sensed in this way and the XLD contrast inverts when the linear polarization is changed by 90°.

Two KNN thin films of 37 nm and 100 nm thicknesses were grown under compressive strain by liquid-delivery spin metal-organic chemical vapor deposition [30, 31] on (110) TbScO₃ (TSO) substrates. The KNN sample of 100 nm thickness had an additional pulsed laser deposited 20 nm thick SrRuO₃ (SRO) intermediate layer [20]. Both samples showed well ordered stripe domains in PFM images that can be found in the Suppl. Information. The strong absorption of soft X-rays presents a challenge for the imaging of epitaxial ferroelectric thin films on substrates that are far above the permissible thickness for transmission experiments. This is especially pertinent for X-ray microscopy of films on oxide substrates at the O K-edge. Hence, the TSO substrates were thinned down to approximately 20 μm with a MultiPrep system (Allied High Tech Products). Subsequently, square and circular membranes of approximately 25 μm diameter with

TSO thicknesses below 1 μm for dichroic imaging were created by Ga-ion focused ion beam (FIB) [32, 33]. The depth and surface morphology of the X-ray transparent windows was monitored in-situ by conventional SEM at varying acceleration voltages. Examples of two adjacent square membranes in the TSO are shown in the inset of Fig. 2(a).

The X-ray absorption of the 37 nm thin KNN sample on TSO was measured in transmission, both at the O K-edge ($1s \rightarrow 2p$) and the Nb $M_{3,2}$ -edges ($3p_{3/2}/3p_{1/2} \rightarrow 4d$) with linear horizontal polarization. The resulting spectra are displayed in Figs. 1(c) and (d), respectively. The O K-edge spectrum shows the usual structure of a transition metal oxide around 529 eV with two crystal-field split absorption peaks due to hybridization, which are highlighted in Fig. 1(c). The O K-edge spectrum also contains a contribution from the TSO substrate, which is inextricable from that of KNN. Nevertheless, the distortion of the NbO_6 octahedra is only accessible by probing the hybridization with the Nb 4d states represented by the lowest energy peaks of the spectrum. The Nb 4d states are also accessed at the Nb $M_{3,2}$ -edges, which are shown in Fig. 1(d). The crystal field also splits these absorption peaks, which is significantly more perceptible than in previous spectroscopical studies of Nb oxides [24, 28].

The ferroelectric domains in the X-ray transparent window for the 100 nm thick KNN film on 20 nm SRO were imaged by STXM at the O K-edge with a FZP of 25 nm outer zone width and 240 μm diameter. The sample was aligned with the linear horizontal (LH) polarization of the incident X-rays from an APPLE II undulator parallel to the $[1\bar{1}0]_{\text{TSO}}$ direction for maximum XLD contrast. The result of an $18 \mu\text{m} \times 18 \mu\text{m}$ STXM scan with horizontally polarized X-rays at the O K-edge is shown in Fig. 2(a). The photon energy corresponding to the t_{2g} hybridization between the O 2p and Nb 4d states maximized the XLD contrast (dashed line in Fig. 1). High XLD with the t_{2g} hybridization has also been observed at the Ti $L_{2,3}$ -edges in ferroelectric PbTiO_3 and PZT [34–36]. This is distinct from the behavior of the O K-edge in BFO in which the e_g states show the maximum XLD contrast [13, 37].

The XLD from the ferroelectric stripe domains is dominant in the STXM image and regions of different superdomains are discernible, which agrees well with the PFM images. The transmission image obtained with a single polarization also shows changes in contrast due to variations in the thickness of the TSO substrate and small circular defects in the film. The variations in the stripe domain periodicity and morphology originate in local decoupling of the 100 nm thick KNN from the TSO substrate and SRO interlayer with strain gradients in growth direction [38, 39].

Non-ferroelectric contributions to the image can be removed by subtraction of images recorded with LH and linear vertically (LV) polarized X-rays. This is demonstrated in Figs. 2(b–d) for the area framed in red in

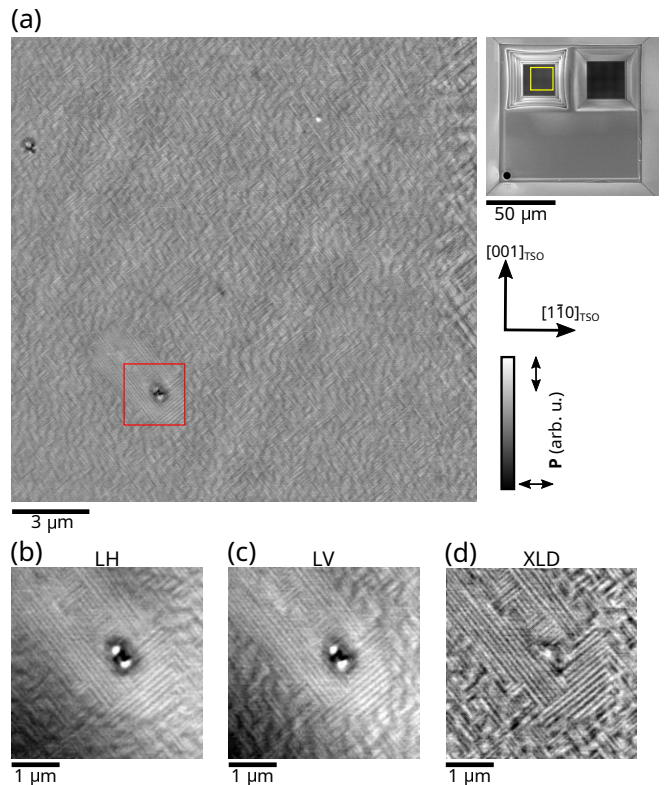


FIG. 2. (a) STXM image of ferroelectric domains in KNN in an $18 \mu\text{m} \times 18 \mu\text{m}$ area. Horizontally polarized X-rays at the O K-edge tuned to the energy of $2p$ - $4d$ t_{2g} hybridization were used. The in-plane components of the ferroelectric polarization \mathbf{P} are in $[001]_{\text{TSO}}$ and $[1\bar{1}0]_{\text{TSO}}$ directions. An SEM image of two X-ray transparent windows in the substrate is shown in the top right with the imaged region framed in yellow. (b–d) Higher resolution images of the framed area in (a) with linear horizontally/vertically polarized X-rays and the corresponding XLD image, emphasizing the ferroelectric domains and suppressing topography contrast.

Fig. 2(a). The contrast of the stripe domains with in-plane ferroelectric polarizations \mathbf{P} along $[1\bar{1}0]_{\text{TSO}}$ and $[001]_{\text{TSO}}$ inverts between Figs. 2(b) and (c). The XLD difference image (Fig. 2(d)) thus separates ferroelectric from structural contributions, making the approach particularly valuable for epitaxial films on substrates with inherent thickness variations. Furthermore, the defects of higher transmittance in the center of the image are removed in the XLD contrast image and reveal their effect on the ferroelectric superdomains surrounding them. The mean stripe periods were 116 nm and 98 nm in the superdomains around the defect. The variation in stripe period and arrangement around the defect suggests a local modification of epitaxial strain, illustrating how STXM can reveal nanoscale coupling between structural defects and ferroelectric order.

The thinner epitaxial film of 37 nm KNN with smaller domains was studied by resonant X-ray scattering (RXS) and holography-assisted CDI in transmission geometry. The spatial resolution of STXM is limited by the spot

size created by the FZP, which is 1.2 times its outer zone width and is around 25 nm for regular operation. Unlike direct imaging methods such as STXM, the spatial resolution of holography-assisted CDI is only restricted by the detected photons at high scattering angles from which the phase can be recovered [40]. Limits for the resolution are set by the distance between sample and detector, the pixel size, the signal-to-noise ratio of the scattering signal and the wavelength of the soft X-rays, which is approximately 2.3 nm at the O K-edge.

The diffraction patterns of RXS were recorded with a Princeton Instruments PI-MTE (MTE-2 1300B) CCD with 1340×1300 pixels of 20 μm size that was positioned 22 cm from the sample. A beamstop of 3.6 mm diameter on a cross was placed in front of the camera to block the intense zero-order X-ray beam.

In the RXS measurements at the O K-edge, the photon energy was scanned in a range of 520–555 eV with LH polarization parallel to $[1\bar{1}0]_{\text{TSO}}$ to identify the resonant interaction of X-rays and ferroelectric polarization. The regularly spaced superdomains in the X-ray transparent window manifested themselves as peaks at the corresponding periodicity of their incorporated ferroelectric stripes in the diffraction pattern (see Fig. 3(a)). The elongation of the diffraction peak indicates a variation of superdomain sizes and potentially non-uniformity of the stripe domains with a mean period of around 50 nm. Even so, the resonant diffraction peaks in the 37 nm thin KNN are significantly more well defined and pronounced than at the same photon energy in the 100 nm thick sample with the SRO interlayer in which the KNN had epitaxially relaxed (see Suppl. Information). The photon energy dependences of the X-ray transmission (XAS) and the RXS signals are displayed in Fig. 3(b). The strongest resonant scattering intensity at 527.6 eV corresponds to the t_{2g} hybridization between O 2p and Nb 4d states (see Fig. 1(c)), which also maximized XLD in STXM. The diffraction peaks of the ferroelectric superdomains are visible with 95% reduced intensity at 2.5 eV higher photon energies. This transition can be assigned to the e_g hybridization of O 2p and Nb 4d states [22, 24].

Further RXS measurements were performed at the M_3 and M_2 -edges of Nb between 360–385 eV. Although the RXS signal was diminished at lower photon energies, the intensities of the diffraction peaks due to the ferroelectric superdomains were still amplified at all the respective transitions (see Fig. 1(d)). The RXS signal at the M_3 t_{2g} transition with the lowest energy is displayed in Fig. 3(c), next to the X-ray transmission and integrated RXS signals in Fig. 3(d).

The diffraction peaks of the ferroelectric superdomains did not show dichroism for circularly polarized X-rays at either the O K-edge or the Nb $M_{3,2}$ edges. Thus, there is no clear indication of polar chirality in the stripe domain walls as was reported for 71° domains in BFO on scandate substrates [37, 41] or in ferroelectric $\text{PbTiO}_3/\text{SrTiO}_3$ superlattices [35, 36], which was confirmed by RXS in reflection geometry. The domain walls in the KNN thin

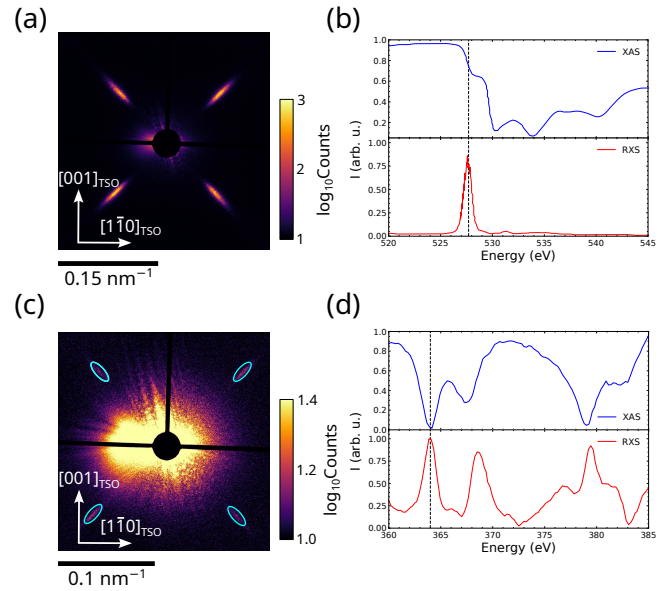


FIG. 3. Resonant X-ray scattering from ferroelectric domains in 37 nm KNN on (110) TSO. (a) RXS at the O K-edge (527.7 eV) shows the presence of diffraction peaks corresponding to the ferroelectric superdomains with ferroelectric stripes of 50 nm mean period in two directions. (b) The normalized X-ray transmission (XAS) and RXS signal from the diffraction peaks are shown. The maximum intensity of diffraction from the superdomains is at the t_{2g} hybridization of the O 2p and Nb 4d states. (c) RXS signal at the Nb M_3 -edge (364 eV) also shows the ferroelectric domains with lower intensity. (d) Intensity of the RXS signal is detectable at the crystal-field split transitions of the Nb $M_{3,2}$ -edges.

film are in all likelihood Ising-like with vanishing polarization.

The conversion of the diffraction peaks pertaining to the ferroelectric domains at the O K-edge into a real space image was accomplished by Fourier transform holography (FTH) [42] with phase retrieval [40], which requires a FTH mask on the sample. This consists of covering the membrane with a metallic Au/Cr multilayer mask, which blocks X-rays except in a circular aperture for the sample and smaller reference holes with diameters in the order of 100 nm. The circular window with which the RXS experiments were performed is shown in Fig. 4(a). The Au/Cr FTH mask was prepared separately, cut from the metallic film as a square and transferred to the KNN film side as shown in Fig. 4(b). A zoomed in view of the FTH mask marked in Fig. 4(b) is shown in Fig. 4(c) after attachment to the KNN surface and Fig. 4(d) shows a view from the opposite side, i.e. through the remaining TSO substrate of sub- μm thickness. The field of view of the holographic image is defined by the diameter of the object hole, which was 1.2 μm for this sample. The imaging of extended areas such as by STXM (Fig. 2(a)) is impossible by FTH with a rigidly fixed mask. On the other hand, the spatial resolution cannot be adversely affected by uncertainties in sample

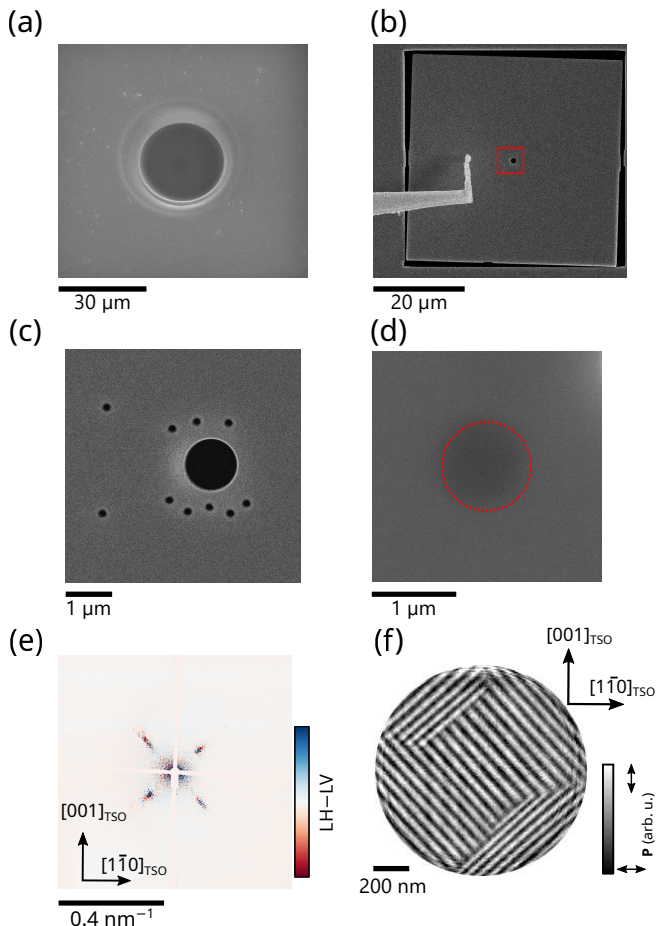


FIG. 4. **Holography-assisted CDI of ferroelectric domains in KNN on TSO.** (a) X-ray transparent window for the RXS measurements in Fig. 3. (b) Square Au/Cr multilayer FTH mask during transfer to the KNN sample. (c) Enlarged view of the FTH mask with object and reference holes after fastening to the sample surface, corresponding to the red framed area in (b). (d) FTH sample from the KNN side. The transparent circular window for the object is circled. (e) Difference in the diffraction patterns with LH and LV polarization obtained at the maximum ferroelectric RXS at the O K-edge (see Figs 3(a-b)). The superdomain diffraction peaks appear with interference fringes. (f) Reconstructed holographic XLD difference image of the ferroelectric superdomains with 57 nm and 44 nm in-plane stripe periods.

positioning as is the case in STXM or ptychography.

A Princeton Instruments PI-MTE: 2048B CCD with 2048×2048 pixels of $13.5 \mu\text{m}$ size was placed 86 mm from the sample and a beamstop of 1 mm diameter was used for the FTH imaging. Illumination of the FTH sample by coherent X-rays at the photon energy providing maximum RXS contrast generated a coherent diffraction pattern, which constitutes an oversampled hologram with interference of X-rays scattered from the ferroelectric stripe domains and diffracted at the reference holes. An XLD map of the ferroelectric domain structure was reconstructed from the difference between diffraction pat-

terns with LH and LV polarized X-rays (see Fig. 4(e)). The result is shown in Fig. 4(f). The field of view includes three superdomains at 90° with stripe periods of 57 nm and 44 nm, which are well ordered due to the epitaxial strain from the TSO. The clearly resolved stripe down to 44 nm period demonstrate that holography-assisted CDI substantially surpasses the resolution limit of STXM. The FTH geometry employed here is directly compatible with emerging real-time imaging schemes such as coherent correlation imaging [43] and with ultrafast pump-probe approaches for reproducible processes at X-ray free-electron laser (XFEL) [44, 45] or high-harmonic generation sources [46], opening prospects for femtosecond imaging of ferroelectric domain dynamics.

In conclusion, the ferroelectric domain structure of epitaxially strained KNN thin films on (110) TSO was imaged at the nanoscale by linear dichroic imaging with STXM and holography-assisted phase retrieval. The ferroelectric stripe domains of the compressively strained KNN films remained intact after back thinning of the substrate to below $1 \mu\text{m}$ for soft X-ray microscopy in transmission. The O K-edge is sensitive to ferroelectric order in KNN due to the hybridization with Nb 4d states, causing strong XLD and RXS signals for the in-plane components of the ferroelectric polarization in $[001]_{\text{TSO}}$ and $[1\bar{1}0]_{\text{TSO}}$ directions. The spatial resolution of STXM was improved upon by reconstruction of the superdomain diffraction peaks from RXS by holography-assisted CDI. The substrate thinning approach demonstrated here is also directly applicable to ptychographic imaging [12, 13, 16, 47]. In future experiments, the spatial resolution and sensitivity of these coherent-diffraction-based imaging approaches will be further enhanced by the availability of single-photon counting area detectors with low readout noise and higher dynamic range in the soft X-ray regime [48]. These improvements will allow detection of faint scattering from ferroelectric domains of metallic oxides with weaker hybridizations. The successful X-ray imaging of ferroelectric order opens possibilities for time-resolved imaging of ferroelectric dynamics, surpassing what has been achieved by stroboscopic PFM with temporal resolutions limited to 100 ns [49]. Using STXM, 50 ps-temporal resolutions can be obtained at synchrotrons with avalanche photo diodes [50, 51] and are already routinely used for the study of magnetization dynamics [47]. Higher resolution CDI imaging methods will be valuable for the investigation of switching and laser induced dynamics [9, 52] at XFEL facilities [45].

ACKNOWLEDGEMENTS

We thank the European Regional Development Fund (ERDF) for funding (Project No. 1.8/15) and Saud Bin Anooz for film growth. The TbScO_3 substrates were grown at the Leibniz-Institut für Kristallzüchtung in the group of Steffen Ganschow. STXM measurements were performed at the MAXYMUS end station at the BESSY

II electron storage ring operated by the Helmholtz-Zentrum Berlin (HZB) für Materialien und Energie. We thank HZB for the allocation of synchrotron-radiation beamtime. FTH assisted CDI measurements were performed with the MAXI endstation of the Max Born Institute at the Veritas and SoftiMAX beamlines of the MAX IV Laboratory. Research conducted at MAX IV, a Swedish national user facility, is supported by the Swedish Research council under contract 2018-07152, the Swedish Governmental Agency for Innovation Systems under contract 2018-04969, and Formas under contract 2019-02496. We acknowledge DESY (Hamburg, Germany), a member of the Helmholtz Association HGF, for the provision of experimental facilities. Supporting

measurements for this research were carried out at PETRA III and we would like to thank S. Chowdhury and M. Hoesch for assistance in using beamline P04. T.A.B. acknowledges funding from the ERDF. We acknowledge funding from the Helmholtz Young Investigator Group Program through Project No. VH-NG-1520, from the Deutsche Forschungsgemeinschaft (DFG, German Research Foundation) through project numbers 462676630 (BiSky), 505818345 (Topo3D), and 49254781 (TRR 360), and the German Federal Ministry of Education and Research (BMBF) under grant number 05K24BCA (Soft-XPCS) within the Röntgen-Ångström Cluster. We thank Mariana Brede for assistance during the STXM measurements.

-
- [1] J. F. Scott, Applications of modern ferroelectrics, *Science* **315**, 954 (2007).
- [2] L. W. Martin and A. M. Rappe, Thin-film ferroelectric materials and their applications, *Nat. Rev. Mater.* **2**, 1 (2016).
- [3] A. Gruverman, M. Alexe, and D. Meier, Piezoresponse force microscopy and nanoferroic phenomena, *Nat. Commun.* **10**, 1661 (2019).
- [4] A. J. Pattison, C. C. S. Pedroso, B. E. Cohen, J. C. Ondry, A. P. Alivisatos, W. Theis, and P. Ercius, Advanced techniques in automated high-resolution scanning transmission electron microscopy, *Nanotechnology* **35**, 015710 (2023).
- [5] R. Moubah, M. Elzo, S. El Moussaoui, D. Colson, N. Jaouen, R. Belkhou, and M. Viret, Direct imaging of both ferroelectric and antiferromagnetic domains in multiferroic BiFeO₃ single crystal using x-ray photoemission electron microscopy, *Appl. Phys. Lett.* **100**, 042406 (2012).
- [6] H. Simons, A. King, W. Ludwig, C. Detlefs, W. Pantleon, S. Schmidt, F. Stöhr, I. Snigireva, A. Snigirev, and H. F. Poulsen, Dark-field x-ray microscopy for multiscale structural characterization, *Nat. Commun.* **6**, 6098 (2015).
- [7] H. Simons, A. B. Haugen, A. C. Jakobsen, S. Schmidt, F. Stöhr, M. Majkut, C. Detlefs, J. E. Daniels, D. Damjanovic, and H. F. Poulsen, Long-range symmetry breaking in embedded ferroelectrics, *Nature materials* **17**, 814 (2018).
- [8] L. von Helden, M. Schmidbauer, S. Liang, M. Hanke, R. Würdenweber, and J. Schwarzkopf, Ferroelectric monoclinic phases in strained K_{0.70}Na_{0.30}NbO₃ thin films promoting selective surface acoustic wave propagation, *Nanotechnology* **29**, 415704 (2018).
- [9] B. Guzelturk, T. Yang, Y.-C. Liu, C.-C. Wei, G. Orenstein, M. Trigo, T. Zhou, B. T. Diroll, M. V. Holt, H. Wen, L.-Q. Chen, J.-C. Yang, and A. M. Lindenberg, Sub-nanosecond reconfiguration of ferroelectric domains in bismuth ferrite, *Adv. Mater.* , 2306029 (2023).
- [10] M. O. Hill Landberg, B. Yan, H. Chen, I. Efe, M. Trassin, and J. Wallentin, Direct imaging of nanoscale ferroelectric domains and polarization reversal in ferroelectric capacitors, *Nano Letters* **25**, 16304 (2025).
- [11] S. O. Hruszkewycz, M. J. Highland, M. V. Holt, D. Kim, C. M. Folkman, C. Thompson, A. Tripathi, G. B. Stephenson, S. Hong, and P. H. Fuoss, Imaging local polarization in ferroelectric thin films by coherent x-ray Bragg projection ptychography, *Phys. Rev. Lett.* **110**, 177601 (2013).
- [12] T. A. Butcher, S. Finizio, L. Heller, N. W. Phillips, B. Sarafimov, C. A. F. Vaz, A. Kleibert, B. Watts, M. Holler, and J. Raabe, Soft x-ray ptychography with sophie: Guide and instrumentation, *Rev. Sci. Instrum.* **96**, 123704 (2025).
- [13] T. A. Butcher, N. W. Phillips, C.-C. Wei, S.-C. Chang, I. Beinik, K. Thånell, J.-C. Yang, S.-W. Huang, J. Raabe, and S. Finizio, Imaging ferroelectric domains with soft-x-ray ptychography at the oxygen K-edge, *Phys. Rev. Appl.* **23**, L011002 (2025).
- [14] H. Jani, J. Harrison, S. Hooda, S. Prakash, P. Nandi, J. Hu, Z. Zeng, J.-C. Lin, C. Godfrey, G. J. Omar, T. A. Butcher, J. Raabe, A. V.-Y. Finizio, S. an dThean, A. Ariando, and P. G. Radaelli, Spatially reconfigurable antiferromagnetic states in topologically rich free-standing nanomembranes, *Nature Materials* **23**, 619 (2024).
- [15] J. Harrison, J. Hu, C. Godfrey, J.-C. Lin, T. A. Butcher, J. Raabe, S. Finizio, H. Jani, and P. G. Radaelli, Room temperature control of axial and basal antiferromagnetic anisotropies using strain, *ACS Nano* **19**, 42118 (2025).
- [16] T. A. Butcher, N. W. Phillips, C.-C. Chiu, C.-C. Wei, S.-Z. Ho, Y.-C. Chen, E. Fröjdth, F. Baruffaldi, M. Carulla, J. Zhang, A. Bergamaschi, C. A. F. Vaz, A. Kleibert, S. Finizio, J.-C. Yang, S.-W. Huang, and J. Raabe, Ptychographic nanoscale imaging of the magnetoelectric coupling in freestanding BiFeO₃, *Adv. Mater.* **36**, 2311157 (2024).
- [17] Y. Saito, H. Takao, T. Tani, T. Nonoyama, K. Takatori, T. Homma, T. Nagaya, and M. Nakamura, Lead-free piezoceramics, *Nature* **432**, 84 (2004).
- [18] Y. Wang, S. Bin Anooz, G. Niu, M. Schmidbauer, L. Wang, W. Ren, and J. Schwarzkopf, Thickness effect on ferroelectric domain formation in compressively strained K_{0.65}Na_{0.35}NbO₃ epitaxial films, *Phys. Rev. Mater.* **6**, 084413 (2022).
- [19] Y. Wang, S. B. Anooz, G. Niu, J. Zhao, M. Schmidbauer, L. Wang, W. Ren, and J. Schwarzkopf, Evolution of domain structure in epitaxial ferroelectric K_{0.5}Na_{0.5}NbO₃ films grown by metal-organic vapor-phase epitaxy, *Phys. Rev. Mater.* **8**, 054409 (2024).

- [20] M. de Oliveira Guimaraes, C. Richter, J. Schwarzkopf, M. Schmidbauer, M. Engl, and S. Slesazek, Ferroelectric switching and temperature-dependent electrical properties of $k_{0.7}na_{0.3}nb_{0.3}$ capacitor devices, *Phys. Rev. Mater.* **10**, 014413 (2026).
- [21] J. Kong, J. Liu, F. Marlton, M. R. V. Jørgensen, and A. Pramanick, Local structural mechanism for phase transition and ferroelectric polarization in the mixed oxide $k_{0.5}na_{0.5}nb_{0.3}$, *Phys. Rev. B* **103**, 184104 (2021).
- [22] L. Douillard, F. Jollet, C. Bellin, M. Gautier, and J. P. Duraud, The electronic structure of $KNbO_3$: an XPS and XAS study, *J. Phys.: Condens. Matter* **6**, 5039 (1994).
- [23] J. Purans, A. Kuzmin, P. Parent, and C. Laffone, Study of the electronic structure of rhenium and tungsten oxides on the O K-edge, *Ionics* **4**, 101 (1998).
- [24] D. Bach, H. Störmer, R. Schneider, D. Gerthsen, and J. Verbeeck, Eels investigations of different niobium oxide phases, *Microsc. Microanal.* **12**, 416 (2006).
- [25] R. Tao, R. Todorovic, J. Liu, R. J. Meyer, A. Arnold, W. Walkosz, P. Zapol, A. Romanenko, L. D. Cooley, and R. F. Klie, Electron energy-loss spectroscopy study of metallic nb and nb oxides, *J. Appl. Phys.* **110**, 124313 (2011).
- [26] M. J. Olszta, J. Wang, and E. C. Dickey, Stoichiometry and valence measurements of niobium oxides using electron energy-loss spectroscopy, *J. Microsc.* **224**, 233 (2006).
- [27] F. Frati, M. O. J. Y. Hunault, and F. M. F. de Groot, Oxygen K-edge x-ray absorption spectra, *Chem. Rev.* **120**, 4056 (2020).
- [28] X. Fang, J.-S. Oh, M. Kramer, A. Romanenko, A. Grassellino, J. Zasadzinski, and L. Zhou, Understanding mechanism of performance improvement in nitrogen-doped niobium superconducting radio frequency cavity, *Mater. Res. Lett.* **11**, 108 (2023).
- [29] Y. Yoneda, T. Kobayashi, T. Tsuji, D. Matsumura, Y. Saitoh, and Y. Noguchi, Local and electronic structures of $NaNbO_3$, $AgNbO_3$, and $KNbO_3$, *Jpn. J. Appl. Phys.* **63**, 09SP12 (2024).
- [30] J. Schwarzkopf, D. Braun, M. Schmidbauer, A. Duk, and R. Wördenweber, Ferroelectric domain structure of anisotropically strained $NaNbO_3$ epitaxial thin films, *J. Appl. Phys.* **115**, 204105 (2014).
- [31] J. Schwarzkopf, D. Braun, M. Hanke, A. Kwasniewski, J. Sellmann, and M. Schmidbauer, Monoclinic M_A domains in anisotropically strained ferroelectric $K_{0.75}Na_{0.25}NbO_3$ films on (110) $TbScO_3$ grown by MOCVD, *J. Appl. Cryst.* **49**, 375 (2016).
- [32] M. Fohler, S. Frömmel, M. Schneider, B. Pfau, C. M. Günther, M. Hennecke, E. Guehrs, L. Shemilt, D. Mishra, D. Berger, S. Selve, D. Mitin, M. Albrecht, and S. Eisebitt, A general approach to obtain soft x-ray transparency for thin films grown on bulk substrates, *Rev. Sci. Instrum.* **88**, 103701 (2017).
- [33] S. Mayr, S. Finizio, J. Reuteler, S. Stutz, C. Dubs, M. Weigand, A. Hrabec, J. Raabe, and S. Wintz, Xenon plasma focused ion beam milling for obtaining soft x-ray transparent samples, *Crystals* **11**, 10.3390/cryst11050546 (2021).
- [34] E. Arenholz, G. van der Laan, A. Fraile-Rodríguez, P. Yu, Q. He, and R. Ramesh, Probing ferroelectricity in $PbZr_{0.2}Ti_{0.8}O_3$ with polarized soft x rays, *Phys. Rev. B* **82**, 140103 (2010).
- [35] P. Shafer, P. García-Fernández, P. Aguado-Puente, A. R. Damodaran, A. K. Yadav, C. T. Nelson, S.-L. Hsu, J. C. Wojdel, J. Íñiguez, L. W. Martin, E. Arenholz, J. Junquera, and R. Ramesh, Emergent chirality in the electric polarization texture of titanate superlattices, *Proc. Natl. Acad. Sci. U.S.A.* **115**, 915 (2018).
- [36] S. W. Lovesey and G. van der Laan, Resonant x-ray diffraction from chiral electric-polarization structures, *Phys. Rev. B* **98**, 155410 (2018).
- [37] J.-Y. Chauleau, T. Chirac, S. Fusil, V. Garcia, W. Akhtar, J. Tranchida, P. Thibaudeau, I. Gross, C. Blouzon, A. Finco, M. Bibes, B. Dkhil, D. D. Khalyavin, P. Manuel, V. Jacques, N. Jaouen, and M. Viret, Electric and antiferromagnetic chiral textures at multiferroic domain walls, *Nat. Mater.* **19**, 386 (2020).
- [38] G. Catalan, B. Noheda, J. McAneney, L. J. Sinnamon, and J. M. Gregg, Strain gradients in epitaxial ferroelectrics, *Phys. Rev. B* **72**, 020102 (2005).
- [39] D. Sando, M. Han, V. Govinden, O. Paull, F. Appert, C. Carrétéro, J. Fischer, A. Barthélémy, M. Bibes, V. Garcia, S. Fusil, B. Dkhil, J. Juraszek, Y. Zhu, X. Ma, and V. Nagarajan, Interfacial strain gradients control nanoscale domain morphology in epitaxial $BiFeO_3$ multiferroic films, *Adv. Funct. Mater.* **30**, 2000343 (2020).
- [40] R. Battistelli, D. Metternich, M. Schneider, L.-M. Kern, K. Litzius, J. Fuchs, C. Klose, K. Gerlinger, K. Bagschik, C. M. Günther, D. Engel, C. Ropers, S. Eisebitt, B. Pfau, F. Büttner, and S. Zayko, Coherent x-ray magnetic imaging with 5 nm resolution, *Optica* **11**, 234 (2024).
- [41] S. Fusil, J.-Y. Chauleau, X. Li, J. Fischer, P. Dufour, C. Léveillée, C. Carrétéro, N. Jaouen, M. Viret, A. Gloter, and V. Garcia, Polar chirality in $BiFeO_3$ emerging from a peculiar domain wall sequence, *Adv. Electron. Mater.* **8**, 2101155 (2022).
- [42] S. Eisebitt, J. Lüning, W. Schlotter, M. Lörger, O. Hellwig, W. Eberhardt, and J. Stöhr, Lensless imaging of magnetic nanostructures by x-ray spectro-holography, *Nature* **432**, 885– (2004).
- [43] C. Klose, F. Büttner, W. Hu, C. Mazzoli, K. Litzius, R. Battistelli, S. Zayko, I. Lemesch, J. M. Bartell, M. Huang, C. M. Günther, M. Schneider, A. Barbour, S. B. Wilkins, G. S. D. Beach, S. Eisebitt, and B. Pfau, Coherent correlation imaging for resolving fluctuating states of matter, *Nature* **614**, 256 (2023).
- [44] C. von Korff Schmising, B. Pfau, M. Schneider, C. M. Günther, M. Giovannella, J. Perron, B. Vodungbo, L. Müller, F. Capotondi, E. Pedersoli, N. Mahne, J. Lüning, and S. Eisebitt, Imaging Ultrafast Demagnetization Dynamics after a Spatially Localized Optical Excitation, *Physical Review Letters* **112**, 217203 (2014).
- [45] A. S. Johnson, D. Perez-Salinas, K. M. Siddiqui, S. Kim, S. Choi, K. Volckaert, P. E. Majchrzak, S. Ulstrup, N. Agarwal, K. Hallman, R. F. Haglund, C. M. Günther, B. Pfau, S. Eisebitt, D. Backes, F. Maccherozzi, A. Fitzpatrick, S. S. Dhesi, P. Gargiani, M. Valvidares, N. Artrith, F. de Groot, H. Choi, D. Jang, A. Katoch, S. Kwon, S. H. Park, H. Kim, and S. E. Wall, Ultrafast X-ray imaging of the light-induced phase transition in VO_2 , *Nat. Phys.* **19**, 215 (2023).
- [46] S. Zayko, O. Kfir, M. Heigl, M. Lohmann, M. Sivis, M. Albrecht, and C. Ropers, Ultrafast high-harmonic nanoscopy of magnetization dynamics, *Nature Communications* **12**, 6337 (2021).

- [47] T. A. Butcher, N. W. Phillips, A. L. Levitan, M. Weigand, S. Wintz, J. Raabe, and S. Finizio, Nanoscale domain-wall dynamics in micromagnetic structures with weak perpendicular anisotropy, *Phys. Rev. B* **111**, L220409 (2025).
- [48] F. Baruffaldi, A. Bergamaschi, M. Boscardin, M. Brückner, T. A. Butcher, M. Carulla, M. Centis Vignali, R. Dinapoli, S. Finizio, E. Fröjdh, D. Greiffenberg, A. Mozzanica, G. Paternoster, N. W. Philips, J. Raabe, B. Schmitt, and J. Zhang, Single-photon counting pixel detector for soft x-rays, *Commun. Phys.* **8**, 321 (2025).
- [49] A. Gruverman, D. Wu, and J. F. Scott, Piezoresponse force microscopy studies of switching behavior of ferroelectric capacitors on a 100-ns time scale, *Phys. Rev. Lett.* **100**, 097601 (2008).
- [50] M. Weigand, S. Wintz, J. Gräfe, M. Noske, H. Stoll, B. Van Waeyenberge, and G. Schütz, Timemaxyne: A shot-noise limited, time-resolved pump-and-probe acquisition system capable of 50 GHz frequencies for synchrotron-based x-ray microscopy, *Crystals* **12**, 10.3390/cryst12081029 (2022).
- [51] S. Finizio, J. B. Bailey, B. Olsthoorn, and J. Raabe, Periodogram-based detection of unknown frequencies in time-resolved scanning transmission x-ray microscopy, *ACS Nano* **16**, 21071 (2022).
- [52] P. Gaal, D. Schmidt, M. Khosla, C. Richter, P. Boesecke, D. Novikov, M. Schmidbauer, and J. Schwarzkopf, Self-stabilization of the equilibrium state in ferroelectric thin films, *Appl. Surf. Sci.* **613**, 155891 (2023).